RSC Advances

PAPER

View Article Online
View Journal | View Issue

Cite this: *RSC Adv.*, 2015, **5**, 13420

Size-controlled synthesis of MCM-49 zeolites and their application in liquid-phase alkylation of benzene with ethylene†

Yanchun Shi, Enhui Xing, Wenhua Xie, Fengmei Zhang,* Xuhong Mu and Xingtian Shu

Received 29th November 2014
Accepted 13th January 2015

DOI: 10.1039/c4ra15470c

www.rsc.org/advances

Size-controlled synthesis of MCM-49 zeolites was achieved *via* topology reconstruction from NaY zeolites with different sizes. SEM images showed that the sizes of the reconstructed H-MCM-49 zeolites were controlled by those of the parent NaY zeolites. Smaller NaY zeolites improved the diffusion of reactants on the parent NaY zeolites during the topology reconstruction, the final H-type zeolites, the relative crystallinity, the BET surface areas, and the number of Brønsted and total acid sites. Moreover, a substantial improvement in both ethylene conversion and ethylbenzene selectivity was observed for the H-type catalyst originating from the smaller NaY zeolite (300 nm) in liquid-phase alkylation of benzene with ethylene. This alkylation performance may provide a new strategy for enhancing both catalytic activity and product selectivity, and our method could be applicable to many diffusion-limited or external surface reactions.

1. Introduction

Ethylbenzene (EB) is an important material for plastic and rubber production. Global demand grew by about 4.1% annually in the period 2009–2014 and is forecast to grow by 3.3% per year over the next decade.[1,2] Compared with the conventional $AlCl_3$ process, the zeolite-based vapor-phase (ZSM-5) and liquid-phase (USY, Beta, MCM-22) EB processes show easy separation, low corrosion, high activity and shape selectivity.[3–8] Because of the low reaction temperature, there are obvious advantages to the liquid-phase process such as high selectivity and long catalyst life. USY zeolite is seldom used because of its relatively inferior EB selectivity and quick deactivation. Owing to their superior activity and selectivity, Beta and MCM-22 zeolites are the most widely used catalysts in commercial liquid-phase alkylation of benzene with ethylene.

Despite their low catalytic activity, MWW zeolites have attracted much attention because of their superior EB selectivity at a lower benzene/ethylene molar ratio with respect to energy input.[9–11] MWW zeolites,[12–18] including PSH-3, ERB-1, SSZ-25, MCM-22, MCM-49, MCM-56, MCM-36, ITQ-1, ITQ-2 and UZM-8, have a MWW structure: 12 MR "cups" (0.71 × 0.71 × 0.91 nm) on the external surface, supercages defined by 12 MR (0.71 nm external diameter × 1.82 nm height) through 10 MR opening windows (0.41 × 0.54 nm), and two-dimensional sinusoidal 10 MR pores (0.41 × 0.54 nm). Some reports[19,20] have claimed that active centers of MWW zeolites are mainly located in the 12 MR cups on the outer surface so that they are more easily accessed during liquid-phase alkylation of benzene with ethylene. Therefore, the 12 MR cups on the outer surface do not restrict the diffusion of reactant toward the active centers. Cheng *et al.*[10] demonstrated that the acid sites on the external surface were the main active centers based on the following comparison tests. 2,4,6-Trimethyl-pyridine (0.62 × 0.56 nm)-doped and undoped H-MCM-22 were used as catalysts in the liquid-phase alkylation of benzene with ethylene at 220 °C with a benzene/ethylene molar ratio of 3.5. Compared with the high ethylene conversion (95.6%) over undoped H-MCM-22, 2,4,6-trimethyl-pyridine-doped H-MCM-22 was almost inactive, giving only 1.4% ethylene conversion. The results indicated that 2,4,6-trimethyl-pyridine is mainly adsorbed on the external surface of H-MCM-22 (12 MR cups) catalysts, and thus the active centers for liquid-phase alkylation of benzene with ethylene are mainly located in 12 MR cups.

To increase the number and accessibility of active centers, equal to improving the alkylation performance, much effort has been devoted to synthesizing MWW zeolites, including preparing small grain sizes,[21] pillaring,[22,23] swelling,[24] interlayer-expansion,[25,26] delaminating,[27,28] and introducing mesopores with basic solution.[29–31] In these methods, it is very important to prepare smaller MWW zeolites to tailor catalytic properties, including high surface activity, short diffusion path lengths, and low carbon deposition. Although most research has focused on materials and conditions to synthesize smaller MWW zeolites *via* conventional hydrothermal treatment, little progress has been made. Hexamethyleneimine (HMI) is an effective structure-

State Key Laboratory of Catalytic Materials and Reaction Engineering, Research Institute of Petroleum Processing, Sinopec, Xueyuan Road 18, Beijing 100083, China. E-mail: zhangfm.ripp@sinopec.com; Tel: +86 010 82368698

† Electronic supplementary information (ESI) available. See DOI: 10.1039/c4ra15470c

directing agent for synthesizing MWW zeolites; therefore, it is difficult to avoid the aggregation of MWW layers, and to achieve size-controlled synthesis of MWW zeolites. Typically, MWW zeolite crystals are sheet-like discs or aggregates of cross-linked discs 2–5 μm in diameter and 10–40 nm in thickness.[32,33] Although the use of cationic polymers could decrease the size of MWW zeolites,[21] this method still requires further consideration because of its economic and environmental impact. Nanosized MCM-22 catalysts demonstrated higher methane conversion, higher benzene yield, higher catalyst stability and lower carbon deposition during methane dehydro-aromatization compared with conventional micro-sized MCM-22 catalysts.[21]

Recently, we investigated the potential of topology reconstruction (direct zeolite-to-zeolite transformation) and succeeded in synthesizing MWW zeolites with FAU parent zeolites,[34] which provided us with a novel strategy to synthesize smaller MWW zeolites and improve their catalytic performance. According to our previous research, MWW zeolites were reconstructed gradually from the exterior to the interior of FAU zeolites, which was clearly demonstrated by the core (FAU)–shell (MWW) co-existing zeolites as intermediates. No extra-framework Al was observed in topology reconstruction, and there was almost no detection of ^{27}Al resonances in the mother liquor. The FAU structure was reconstructed into the MWW structure without complete disappearance of crystalline phase, which led us to consider whether the sizes of target MWW zeolites could be controlled by the original sizes of the parent FAU zeolites *via* topology reconstruction. Through this strategy, it may be easy to synthesize smaller MWW zeolites and improve their alkylation performance. In this work, we intentionally select NaY zeolites with different sizes as parent zeolites for the size-controlled synthesis of MWW zeolites. We also examine the effects of the size of the parent NaY zeolites on the topology reconstruction and the liquid-phase alkylation of benzene with ethylene over the reconstructed MWW catalysts. Our method may be suitable for the size-controlled synthesis of target MWW zeolites.

2. Experiments

2.1 Synthesis of MCM-49 and preparation of H-type catalysts

Topology reconstruction from FAU to MWW structure. All materials were used as purchased. Commercial NaY zeolites (Table 1; average sizes: 1000, 500, and 300 nm, Sinopec Catalyst Co., Ltd) were mixed in a conical flask with NaOH (96 wt%, Beijing Chemical Works), HMI (98 wt%, TCI), solid silica gel (90 wt% SiO_2, Qingdao Haiyang Chemical Co., Ltd.), and deionized water. The molar ratios of the batch composition were: $SiO_2/Al_2O_3 = 25$, $NaOH/SiO_2 = 0.18$, $HMI/SiO_2 = 0.3$ (300 nm: $HMI/SiO_2 = 0.2$), $H_2O/SiO_2 = 15$. The order of addition was deionized water, NaOH, silica gel, NaY zeolite and HMI with continuous stirring. Topology reconstruction was carried out in a Teflon-lined autoclave at 145 °C and 30 rpm. As a comparison for sample 1, MCM-49 zeolite was synthesized in the 1 m^3 demonstration unit at Hunan Jianchang Petrochemical Company (Sinopec) *via* temperature-controlled phase transfer hydrothermal synthesis.[35] The molar ratios of the batch composition were: $SiO_2/Al_2O_3 = 25$, $NaOH/SiO_2 = 0.18$, $HMI/SiO_2 = 0.3$, $aniline/SiO_2 = 0.2$, $H_2O/SiO_2 = 15$. The synthesis was carried out at 145 °C for 72 h with a stirring speed of 15 Hz. The products were recovered by filtration, washed with deionized water until they reached pH 7 and dried in an oven at 100 °C overnight to remove physically adsorbed water molecules.

H-type zeolites. H-type zeolites were prepared by two repetitions of liquid-phase ion exchange with NH_4NO_3 solution at 90 °C for 2 h. The products were filtered and dried at 100 °C overnight, and calcined at 550 °C for 6 h, to obtain the corresponding H-type zeolites with a Na_2O content of less than 0.05 wt%. The mass ratio composition of the MCM-49 zeolites : NH_4NO_3 : deionized water was 1 : 1 : 20. According to the sizes of the parent NaY zeolites (1000, 500, and 300 nm), the products were named HYM, HYM500 and HYM300, respectively.

Catalyst preparation. The NH_4-type samples (70 wt%) and Al_2O_3 (30 wt%) were mixed and extruded. Al_2O_3, which showed almost no activity for the liquid-phase alkylation of benzene with ethylene, was used as binder to increase the mechanical strength of the catalysts. The extruded catalysts were crushed with dimensions of 16–20 mesh to collect particles that were then subjected to calcination at 550 °C for 6 h to obtain the corresponding H-type catalysts.

2.2 Characterization

Intermediate phase characterization. X-ray diffraction (XRD) patterns of samples were collected on an X'pert X-ray diffractometer (PANalytical Corporation, Netherlands) with filtered Cu

Table 1 Topology reconstruction from NaY to MCM-49 zeolites

	Parent zeolites			Conditions of topology reconstruction[a]					Products		
Samples	SiO_2/Al_2O_3	Na_2O (wt%)	Size (nm)	SiO_2/Al_2O_3	HMI/SiO_2	$NaOH/SiO_2$	H_2O/SiO_2	Time (h)	SiO_2/Al_2O_3[b]	XRD	R.C.[c] (%)
1	—	—	—	25	0.3	0.18	15	72	23	MCM-49	100
2	5.0	10.5	1000	25	0.3	0.18	15	88	21	MCM-49	100
3	5.0	10.1	500	25	0.3	0.18	15	72	21	MCM-49	102
4	5.0	9.8	300	25	0.2	0.18	15	72	21	MCM-49	103
5	5.0	9.8	300	25	0.3	0.18	15	72	21	ZSM-35	—

[a] All crystallization temperatures, 145 °C. [b] SiO_2/Al_2O_3 of products by XRF analysis. [c] Relative crystallinity (%): sample 1 synthesized by conventional hydrothermal method defined as R.C. = 100%.

Kα radiation at a tube current of 40 mA and a voltage of 40 kV. The scanning range of 2θ was 5–35°. The relative crystallinity of the samples was calculated according to the sum of the peak intensities at 2θ of 14.3°, 22.7°, 23.7° and 26.0°. ^{29}Si MAS NMR experiments were performed on a Bruker AVANCE III 500WB spectrometer at a resonance frequency of 99.3 MHz using a 7 mm double-resonance magic-angle spinning (MAS) probe. The MAS speed was 5 kHz in all experiments, and a typical $\pi/6$ pulse length of 1.8 μs was used for ^{29}Si resonance. The chemical shift of ^{29}Si was referenced to tetramethylsilane (TMS). ^{27}Al MAS NMR experiments were performed on a Bruker AVANCE III 600WB spectrometer at a resonance frequency of 156.4 MHz using a 4 mm double-resonance MAS probe at a sample-spinning rate of 13 kHz. The chemical shift of ^{27}Al was referenced to 1 M aqueous $Al(NO_3)_3$. ^{27}Al MAS NMR spectra were recorded by the small-flip angle technique using a pulse length of 0.4 μs ($<\pi/15$) and a recycle delay of 1 s.

Characterization of H-MCM-49 zeolites. The crystal morphology was measured on a Quanta (FEI) scanning electron microscope (SEM). The elemental analyses of the solids were performed on a MagiX (Philips) X-ray fluorescence (XRF) spectrometer. Nitrogen adsorption–desorption isotherms were recorded on a Micromeritics ASAP 2010 instrument. The samples were out gassed under vacuum at 90 °C for 1 h and at 350 °C for 15 h. The total surface area was obtained by using the BET equation using the relative pressure range of 0.05–0.16 in the nitrogen adsorption isotherm as the range of linearity (molecular cross-sectional area for N_2 of 0.162 nm^2). The micropore volume was calculated by the *t*-plot method.

Acidity characterization. The acidity of H-type zeolites was measured by temperature programmed desorption (TPD) and Fourier transform infrared (FTIR) spectrometry, using NH_3 and pyridine as probe molecules, respectively. TPD of ammonia (NH_3-TPD) was carried out in an Autochem II 2920 unit equipped with a thermal conductivity detector. The samples (~200 mg, 20–40 mesh) were pretreated at 600 °C in a flow of He (25 cm^3 min^{-1}) for 60 min. Afterwards, pure NH_3 (25 cm^3 min^{-1}) was adsorbed at room temperature for 30 min followed by He purging at 100 °C for 90 min. Desorption of ammonia was monitored in the range of 100–600 °C using a heating rate of 10 °Cmin^{-1}. Py-FTIR spectra were obtained on a FTS3O00 FT-IR spectrometer with 64 scans and a resolution of 4 cm^{-1}. Self-supporting thin wafers were pressed and placed in a quartz IR cell with CaF_2 windows, which was used in pyridine adsorption studies. Prior to the measurements, each sample was dehydrated under vacuum (10^{-3} Pa) at 350 °C for 1 h, and then cooled to 50 °C for pyridine adsorption. The IR spectra of the samples before pyridine adsorption were recorded at different temperatures (200 and 350 °C), and after adsorbing pyridine for 10 s, the samples were purged under vacuum (10^{-3} Pa) and then heated at a rate of 10 °C min^{-1}. Next, the IR spectra of pyridine on samples were recorded at different temperatures (200 and 350 °C). All the spectra presented in this work are difference spectra.

2.3 Liquid-phase alkylation of benzene with ethylene

The liquid-phase alkylation of benzene with ethylene was carried out in a stainless-steel fixed bed reactor. The catalyst (8 mL) was placed in the center of the reactor and it was nitrogen-purged. Benzene was pumped into the reactor to fill the bed fully under reaction pressure, and then the temperature was raised to 200 °C before ethylene was introduced. The alkylation conditions were as follows: pressure of 3.5 MPa, a weight hourly space velocity (WHSV) of benzene of 3 h^{-1}, a benzene/ethylene molar ratio of 12/1, and temperatures of 200 to 260 °C. The reaction products were not collected until every temperature point lasted at least for 15 h, three times a day, which ensured that the reaction was completely steady. The reaction products were analyzed by an Agilent 6890 gas chromatograph (GC) equipped with a flame ionization detector and a capillary column. The alkylation of benzene with ethylene is a consecutive reaction, and the reaction products consisted of ethylbenzene (EB), *para*-diethylbenzene (*p*-DEB), *ortho*-diethylbenzene (*o*-DEB), *meta*-diethylbenzene (*m*-DEB), triethylbenzenes (TEB), and other by-products (diphenylethane). The ethylene conversion, EB selectivity, DEB selectivity and DEB distribution of the selectivity were calculated based on the following formulas.

$$H = x_{EB}/M_{EB} + 2x_{DEB}/M_{DEB} + 3x_{TEB}/M_{TEB} + x_{diphenylethane}/M_{diphenylethane}$$

$$x_{DEB} = x_{p\text{-}DEB} + x_{o\text{-}DEB} + x_{m\text{-}DEB}$$

where M is the molar mass (g mol^{-1}), x is the mass percentage concentration (wt%) from GC analysis, and H is the molar number percentage concentration (mol%) of ethyl.

(1) Ethylene conversion (%): $C_{ethylene} = H/(H + x_{ethylene}/M_{ethylene}) \times 100$

(2) EB selectivity (%): $S_{EB} = x_{EB}/(x_{EB} + x_{DEB} + x_{TEB} + x_{diphenylethane}) \times 100$

(3) DEB selectivity (%): $S_{DEB} = x_{DEB}/(x_{EB} + x_{DEB} + x_{TEB} + x_{diphenylethane}) \times 100$

(4) DEB distribution of selectivity:

$m(p\text{-DEB})/m(DEB) = x_{p\text{-}DEB}/(x_{p\text{-}DEB} + x_{m\text{-}DEB} + x_{o\text{-}DEB}) \times 100$

$m(m\text{-DEB})/m(DEB) = x_{m\text{-}DEB}/(x_{p\text{-}DEB} + x_{m\text{-}DEB} + x_{o\text{-}DEB}) \times 100$

$m(o\text{-DEB})/m(DEB) = x_{o\text{-}DEB}/(x_{p\text{-}DEB} + x_{m\text{-}DEB} + x_{o\text{-}DEB}) \times 100$

3. Results and discussions

3.1 Synthesis of MCM-49 zeolites *via* topology reconstruction

NaY parent zeolites (SiO_2/Al_2O_3 = 5.0) with different sizes (average sizes: 1000, 500, and 300 nm) were used to provide all Al and some Si in the following experiments. Supplementary Si was provided by solid silica gel to meet the mass balance for the synthesis of high-silica MCM-49 zeolites. The chemical compositions of the parent and target samples are listed in Table 1. First, the SiO_2/Al_2O_3 molar ratios of MCM-49 zeolites, which were obtained by the topology reconstruction of NaY zeolites with different sizes, were lower than those obtained by initial feeding of 25. All MCM-49 zeolites had high relative crystallinity compared with MCM-49 synthesized *via* the conventional hydrothermal method (relative crystallinity: 100%). Second, it is worth noting that it took longer for NaY

(1000 nm) to complete the whole reconstruction process (Sample 2, 88 h in Table 1 and Fig. 1a) than NaY (500 nm, Sample 3, 72 h in Table 1 and Fig. 1b) under identical conditions. Additionally, despite the crystallization time being the same, less HMI (HMI/SiO_2 = 0.2) was needed for 300 nm NaY to accomplish topology reconstruction than that needed for 500 nm NaY (HMI/SiO_2 = 0.3), which also showed that the pure FER zeolite was formed thermodynamically with HMI/SiO_2 of 0.3 (Table 1, sample 5).

XRD patterns of the as-made samples during the topology reconstruction are shown in Fig. 1. The patterns of topology reconstruction from FAU (1000 and 500 nm) to MWW (MCM-49, SiO_2/Al_2O_3 > 20) were similar; the diffraction peaks of NaY decreased at 48 h, and peaks corresponding to MCM-49 emerged and increased with increasing crystallization time. Clearly, the FAU-MWW zeolites were the intermediates during the topology reconstruction. Furthermore, at 48 h, there were stronger diffraction peaks for MCM-49 in Fig. 1b for the 500 nm parent NaY zeolite than those in Fig. 1a for the 1000 nm parent NaY zeolite. There are two points that should be emphasized. First, there was a large amount of amorphous phase observed by XRD during the topology reconstruction. The amorphous phase was associated with the solid silica gel used to provide extra SiO_2. The amount of solid silica gel accounted for about 75 wt% of the total feeding, explaining the large amount of amorphous phase. For example, from 48 to 72 h in Fig. 1a, the amorphous phase decreased and finally disappeared at 88 h; therefore, the amorphous SiO_2 was gradually consumed during the topology reconstruction and completely consumed at the end of the topology reconstruction. Second, all MCM-49 zeolites were formed *via* the topology reconstruction from NaY zeolites with different sizes, and XRD patterns showed that MCM-22P with 2D structure did not form. During the topology reconstruction, there were no typical diffraction peaks of MCM-22P, such as the typical (002) diffraction peak located at 2θ of 6.6°.[33] MCM-49 with a 3D structure was reconstructed from NaY zeolites with a 3D structure. In other words, the topology reconstruction proceeded *via* partial destruction without complete destruction of the 3D connections. This is the only plausible way that the size-controlled synthesis of MCM-49 zeolites could be achieved efficiently from parent zeolites with different sizes.

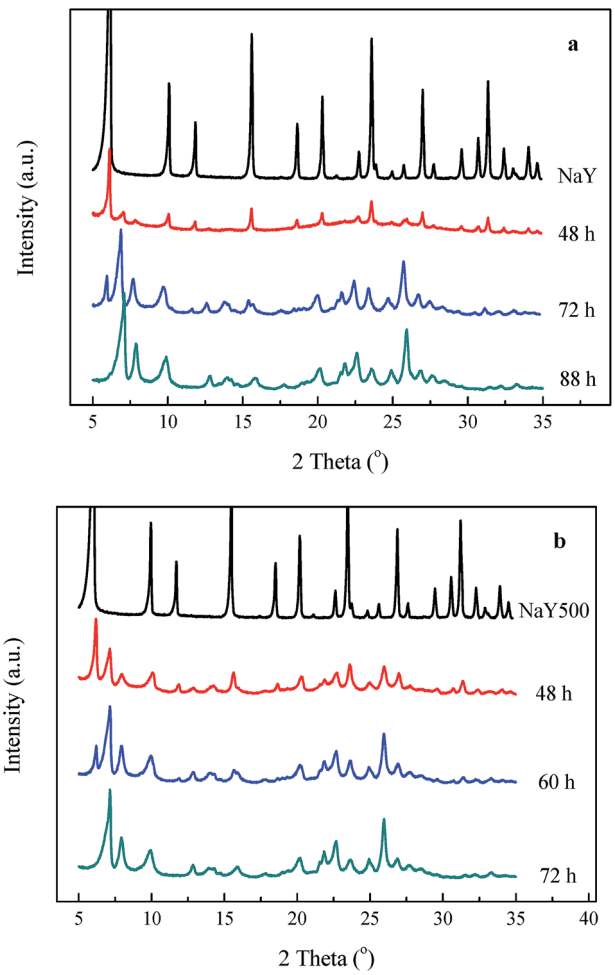

Fig. 1 XRD patterns of as-synthesized samples obtained from the topology reconstruction of FAU zeolites of different sizes (NaY: a, 1000 nm; b, 500 nm) at various crystallization time.

The $^{29}Si/^{27}Al$ MAS NMR spectra of samples obtained *via* the topology reconstruction from NaY (300 nm) at various crystallization time have been explained in detail in our previous paper.[32] Similarly, the $^{29}Si/^{27}Al$ MAS NMR spectra were employed to investigate the chemical environments of the framework Si/Al in topology reconstruction processes from two other parent NaY zeolites (1000 and 500 nm). It appears that there were similarities in the topology reconstruction of the three kinds of parent zeolites. Fig. 2a and b shows that for NaY there were the typical resonances of framework Si that were assigned as follows:[36] −88 ppm Si(3Al), −95 ppm Si(2Al), −100 ppm Si(1Al), and −105 ppm Si(0Al). The resonances of the FAU framework Si were decreased by the destruction of the FAU structure at 48 h, and with further crystallization time, the resonances of the MCM-49 zeolite at around −100 and −105 to −119 ppm (ref. 13) became clear from 48 to 88 h. Eventually, the MWW framework was fully formed with the complete disappearance of the FAU framework Si. The results clearly revealed the FAU destruction and MWW growth during the topology reconstruction, in which the hydrothermal destruction of the FAU structure should be the rate-determining step for the whole topology reconstruction. Additionally, there are also some differences. Fig. 2a shows the transformation of the framework Si from NaY (1000 nm) to MCM-49 zeolite, and at crystallization time from 48 to 72 h, there were no resonances between −113 and −119 ppm. Fig. 2b shows two strong resonances at −115 and −119 ppm at 48 h for the transformation from NaY (500 nm) to MCM-49 zeolite that were mainly ascribed to Si(0Al). This indicates that NaY (500 nm) was easier to reconstruct into MCM-49 than NaY (1000 nm), which was in accordance with the XRD results.

Furthermore, the transformations of framework Al in the topology reconstruction are shown in Fig. 2c and d. With the increase of the crystallization time, the ^{27}Al MAS NMR resonances at 50, 56 and 60 ppm (MWW) gradually increased with the decrease of the resonance at 62 ppm (FAU), which showed clearly that the framework Al of the FAU structure was gradually

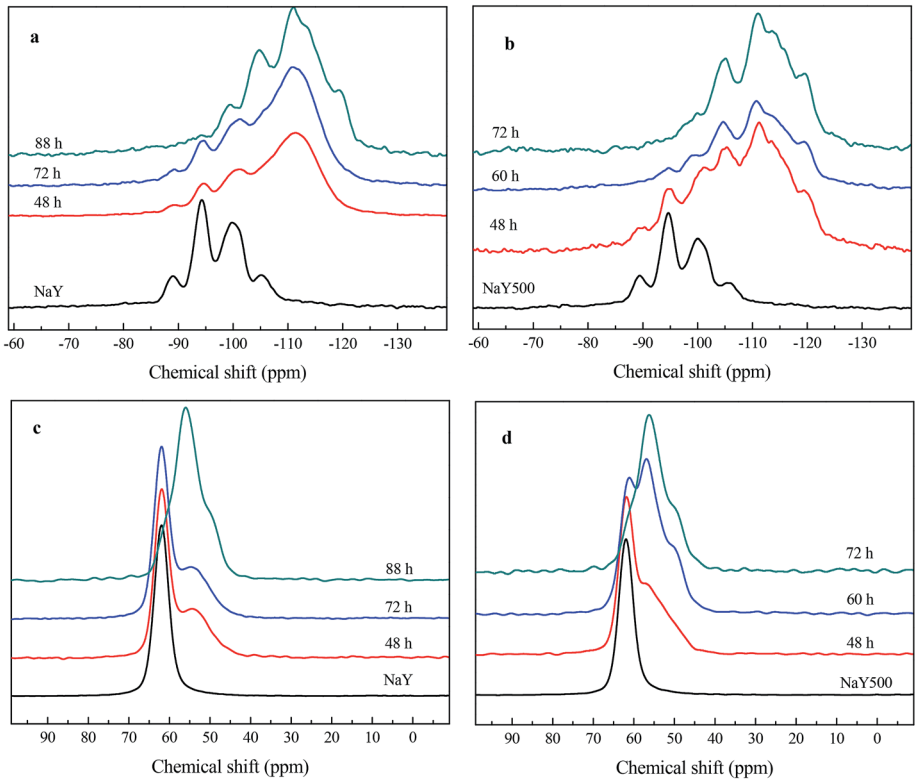

Fig. 2 $^{29}Si/^{27}Al$ MAS NMR spectra of as-synthesized samples obtained from the topology reconstruction of FAU zeolites of different sizes (a: ^{29}Si NMR-NaY 1000 nm; b: ^{29}Si NMR-NaY 500 nm; c: ^{27}Al NMR-NaY 1000 nm; d: ^{27}Al NMR-NaY 500 nm) at various crystallization time.

transformed to the framework Al of the MWW structure by Si insertion. Moreover, Al transformation for NaY (500 nm) was faster than that of NaY (1000 nm) from 48 to 72 h. During the entire process, there was no extra-framework Al formation, which demonstrated direct transformation from the FAU to the MWW structure.

The XRD and NMR results suggest that the smaller sizes of the starting NaY zeolites presented better diffusion, which helped the other reactants (HMI, NaOH and silica source) to diffuse to achieve the topology reconstruction. This could mean that the reconstruction of the smaller parent zeolites to the target zeolites is easier. The direct transformation from NaY to MCM-49 zeolites, defined as topology reconstruction, indicated that size control of the target MWW zeolites was possible. Through this method, size-controlled synthesis of MCM-49 zeolite can be easily achieved, and it was critical to tailor the catalytic performance of MWW zeolites in the liquid-phase alkylation of benzene with ethylene.

3.2 Physicochemical properties of H-type zeolites

XRD patterns of H-type zeolites are presented in Fig. 3. The similarity in the XRD patterns between the as-synthesized samples and H-type zeolites indicated that the reconstructed MCM-49 zeolites were mostly retained after NH_4^+ ion-exchange and calcination. Furthermore, the relative crystallinity was higher for all H-type products (HYM: 100%; HYM: 105%; HYM300: 108%) than the corresponding Na-MCM-49 zeolites in Table 1, which indicated that the MWW structure was perfectly preserved during the ion-exchange process.

Our initial aim was to achieve size-controlled synthesis of MWW zeolites and to tailor their alkylation performance. Fig. 4 shows SEM images of parent zeolites with different average sizes (1000, 500 and 300 nm) and the increase in the volume of the corresponding products. The sizes of HYM were larger than 1000 nm. The sizes of HYM500 were close to 1000 nm. The sizes of HYM300 were smaller than 1000 nm. Obviously, the sizes of

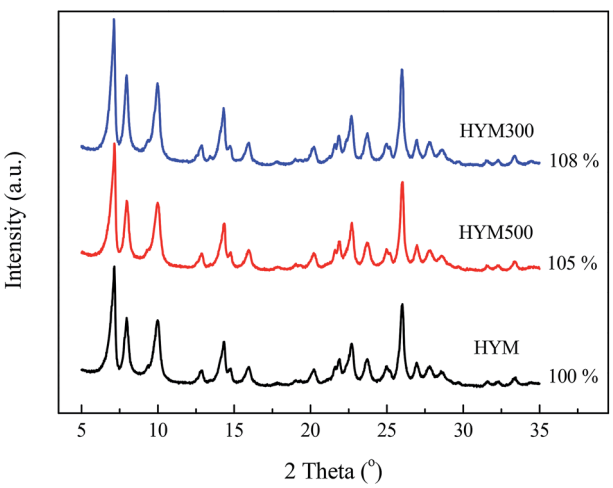

Fig. 3 XRD patterns of H-type zeolites.

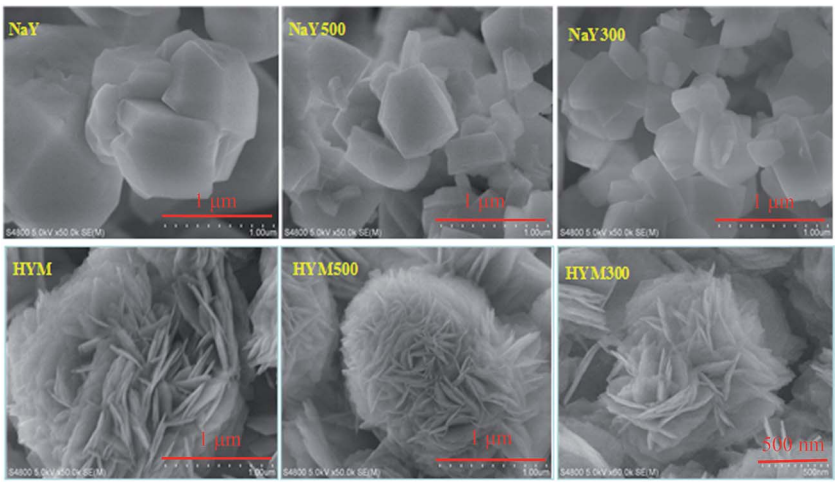

Fig. 4 SEM images of NaY and corresponding H-type zeolites.

the products can be controlled by the size of the parent zeolite *via* the transformation from FAU to MWW structure, even though the volume increases. Therefore, these results demonstrate a new route for achieving our initial objective, and for the size control of the target product *via* topology reconstruction. Generally speaking, smaller target zeolites may offer a larger number of active centers on the exterior surface and better accessibility to the active centers because the diffusion is less limited, which is beneficial for liquid-phase alkylation of benzene with ethylene.

Table 2 shows no obvious changes for SiO_2/Al_2O_3 ratios in 21 of the H-type zeolites, as well as in Na-type zeolites. The texture properties of H-type zeolites were characterized by the nitrogen adsorption–desorption method. The data showed both the surface areas and total pore volumes increased slightly as the sizes of the parent zeolites decreased. The BET surface areas were 465 $m^2 g^{-1}$ for HYM < 489 $m^2 g^{-1}$ for HYM500 < 496 $m^2 g^{-1}$ for HYM300. The micro surface areas were 406 $m^2 g^{-1}$ for HYM < 408 $m^2 g^{-1}$ for HYM500 < 410 $m^2 g^{-1}$ for HYM300. The external surface areas were 59 $m^2 g^{-1}$ for HYM < 81 $m^2 g^{-1}$ for HYM500 < 86 $m^2 g^{-1}$ for HYM300. The total volumes were 0.44 $cm^3 g^{-1}$ for HYM < 0.51 $cm^3 g^{-1}$ for HYM500 < 0.54 $cm^3 g^{-1}$ for HYM300. Generally, the micro surface areas and micro volumes showed no substantial differences. The effect of the parent NaY zeolite size was greater on the external surface areas and external pore volumes, which contributed to the increase in the BET surface areas and the total pore volumes, although it did not affect the micropore data. HYM300 possessed the largest surface area and pore volume, and HYM had the smallest surface area and pore volume in Table 2, demonstrating the effect of the parent zeolite size on the texture properties of the final H-type zeolites. This can be explained by the decreased crystal size of MWW zeolites, which contributes little to the increase in the micropore properties, although it does contribute to the external pore properties.

There was a similar trend in the acidity of H-type zeolites obtained by topology reconstruction. Fig. 5 presents the NH_3-TPD results. For all reconstructed H-type zeolites, there were two desorption peaks at around 215 and 400 °C, corresponding to the weak and strong acid sites, respectively. HYM300 contained the highest number of acid sites, as characterized by NH_3-TPD and Py-FTIR (Table 3 and Fig. S1 and S2 in ESI†). The order of the number of acid sites was HYM300 > HYM500 > HYM. For Brønsted acid sites the results were 620 μmol g^{-1} (HYM300) > 501 μmol g^{-1} (HYM500) > 365 μmol g^{-1} (HYM) at 200 °C; and 544 μmol g^{-1} (HYM300) > 447 μmol g^{-1} (HYM500) > 324 μmol g^{-1} (HYM) at 350 °C. The total number of Brønsted and Lewis acid sites exhibited similar variations at 200 and 350 °C, although there were some fluctuations in the number of Lewis acid sites in all products. These results also demonstrated that smaller zeolites possessed a higher number of Brønsted acid sites, which may offer a higher number of active centers in the liquid-phase alkylation of benzene with ethylene.

Generally, the number of total acid sites was strongly dependent on the sizes of the probe molecules. With pyridine as the probe molecule, HYM300 showed the highest number of acid sites of all the products, and HYM showed the lowest number. However, the NH_3-TPD results showed only slight differences (Fig. 5). This may be because HYM300 possessed the highest surface area and pore volume. Furthermore, the pyridine molecules have a kinetic diameter of 0.58 nm, which results in a higher mass transfer restriction within the micropore channels than NH_3 molecules (kinetic diameter 0.26 nm). The XRF results confirmed that the reconstructed MCM-49 zeolites had almost the same SiO_2/Al_2O_3 ratios of 21, which indicated that they may have same number of acid sites; however the number of acid sites determined by both NH_3-TPD and Py-FTIR increased as the H-type zeolites size decreased, which is usually observed in nanosized zeolite catalysts. We propose that the increased number of acid sites increases the number of active centers and improves the accessibility of active centers for alkylation. All results indicate that HYM300 may possess superior accessibility of active centers, which is very important for zeolites to act as catalysts in the liquid-phase alkylation of benzene with ethylene.

Table 2 Texture properties of H-type zeolites

Samples	SiO_2/Al_2O_3	S_{BET} ($m^2\ g^{-1}$)	S_{micro} ($m^2\ g^{-1}$)	S_{ext} ($m^2\ g^{-1}$)	V_{micro} ($cm^3\ g^{-1}$)	V_{total} ($cm^3\ g^{-1}$)
HYM	21	465	406	59	0.20	0.44
HYM500	21	489	408	81	0.19	0.51
HYM300	21	496	410	86	0.19	0.54

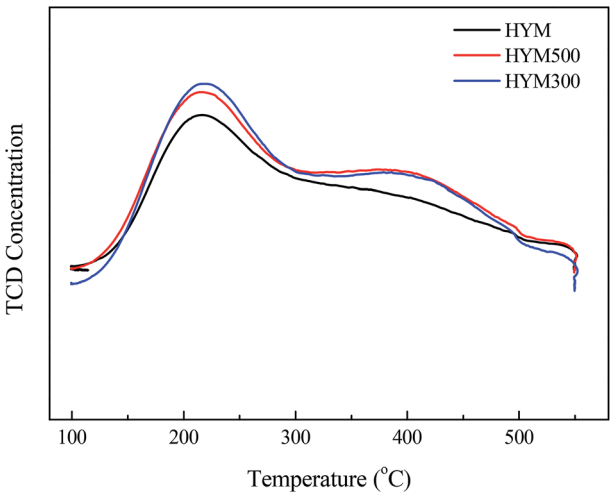

Fig. 5 NH_3-TPD curves of H-type zeolites.

3.3 Liquid-phase alkylation of benzene and ethylene over H-type catalysts

Ethylene conversion and EB selectivity. The alkylation of benzene with ethylene is a consecutive reaction with EB as the target product. Therefore, the trade-off between ethylene conversion and EB selectivity must be carefully considered; usually, improved ethylene conversion is accompanied by decreased EB selectivity. The alkylation performance of catalysts synthesized through topology reconstruction from NaY zeolites is shown in Fig. 6a and b. For the HYM catalyst, ethylene conversion was improved from 89.5% to 98.8% by increasing the temperature from 200 to 260 °C, although the EB selectivity decreased from 95.4% to 94.5%. Similarly, in the HYM500 catalyst, increasing the temperature from 200 to 260 °C increased ethylene conversion from 95.4% to 99.4% and decreased EB selectivity from 95.7% to 94.9%. Although EB selectivity slightly decreased from 95.8% to 95.4%, HYM300 showed a steady ethylene conversion of 98.4% from 200 to 250 °C, and 99.3% at the final temperature of 260 °C. It is expected that the ethylene conversion would increase with the temperature, and that the EB selectivity would decrease.

The HYM300 catalyst that originated from the 300 nm NaY zeolite showed the best ethylene conversion and EB selectivity of all the H-type catalysts, whereas the catalyst from the largest zeolite (1000 nm) exhibited the poorest performance. Fig. 6a and b shows that the order of ethylene conversion in catalysts was HYM300 > HYM500 > HYM, which was the same as the order of EB selectivity. These results strongly suggest that the small HYM300 catalyst possessed the highest ethylene conversion because of their higher BET surface areas, smaller sizes, and larger number of active centers. Therefore, a larger number of active centers were exposed to the reactants and there were more opportunities for the reagents to access the active centers (12 MR cups) on the outer surface. The 12 MR cups on the outer surface did not restrict the diffusion of the reactants toward the active centers to improve ethylene conversion and EB selectivity. Moreover, the increase in acid sites, as determined by Py-FTIR, improved the accessibility of the acid sites to pyridine. Therefore, as the size of the H-type catalysts decreases, the accessibility of the active centers to benzene molecules is improved and this enhances the ethylene conversion and EB selectivity. Furthermore, there is almost no trade-off between ethylene conversion and EB selectivity in the consecutive reaction as the size of the H-type catalysts decreases. This is mainly attributed to the better diffusion of the reactant in smaller H-type zeolites. In addition, because of the same ethylene feeding, the increase in activity of smaller catalysts means that more EB is produced, decreasing the amount of ethylene available to react with EB to produce DEB, TEB and other by-products. Therefore, the results highlight an important strategy for designing alkylation catalysts, which demonstrates that an excellent catalyst, with smaller particles, higher relative crystallinity, higher BET surface areas and a larger number of acid sites offers more opportunities for benzene to access active centers, and can help

Table 3 Acid properties of H-type zeolites

	200 °C		350 °C	
Samples	Lewis acid ($\mu mol\ g^{-1}$)	Brønsted acid ($\mu mol\ g^{-1}$)	Lewis acid ($\mu mol\ g^{-1}$)	Brønsted acid ($\mu mol\ g^{-1}$)
HYM	342	365	263	324
HYM500	271	501	212	447
HYM300	343	620	276	544

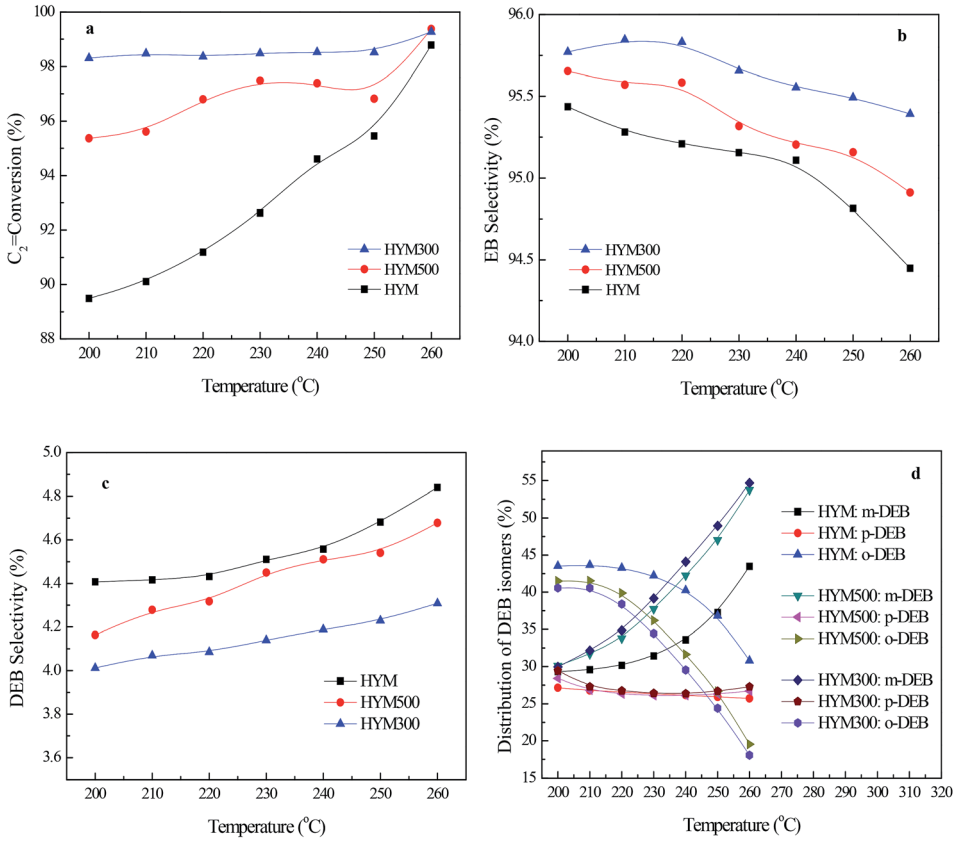

Fig. 6 Ethylene conversion (%, a), ethylbenzene selectivity (%, b), DEB selectivity (%, c), and DEB distribution (%, d) of H-type catalysts. Liquid-phase alkylation conditions: catalyst, 8 mL; T = 200 to 260 °C; p = 3.5 MPa; benzene WHSV^{-1} = 3.0 h^{-1}; benzene/ethylene molar ratio = 12.0.

decrease the trade-off between high ethylene conversion and high EB selectivity.

DEB selectivity and DEB distributions. Fig. 6c and d shows DEB selectivity and DEB distributions over H-type catalysts in the liquid-phase alkylation of benzene with ethylene. The DEB selectivity for all H-type catalysts increased with the temperature and the size of the zeolite (Fig. 6c). The smaller the MCM-49 zeolite, the smaller amount of DEB was produced and the better the EB selectivity. At low temperatures, all H-type catalysts showed a high degree of selectivity for *o*-DEB (Fig. 6d), and the amount of *o*-DEB decreased when the temperature increased from 200 to 260 °C. In contrast, a low degree of selectivity for *m*-DEB was achieved. *p*-DEB has the smallest molecular diameter of the three DEB isomers, whereas space-filling models show that *o*-DEB has the most favorable configuration for the active centers of H-type catalysts. As the temperature increased, the amount of *m*-DEB produced by the isomerization of *o*-DEB increased, whereas the selectivity of *p*-DEB was almost unchanged. Additionally, the proportion DEB isomers moved toward the thermodynamic equilibrium values and the quality ratios of DEB isomers (*m*-DEB : *p*-DEB : *o*-DEB) were maintained as 64 : 30 : 6.[10] Generally, generating less DEBs allows better EB selectivity to be achieved. Therefore, the HYM300 catalyst reconstructed from NaY (300 nm) showed the lowest DEB selectivity and the highest EB selectivity accompanying the highest ethylene conversion.

Liquid-phase alkylation of benzene with ethylene over the conventional H-MCM-49 and HYM300 catalysts. First, we measured the properties of the conventional H-MCM-49 catalyst, the relative crystallinity of which was set as 100%. By using the conventional hydrothermal method, the SiO_2/Al_2O_3 of H-MCM-49 was determined to be 23 by XRF analysis. The BET, micro and external surface areas were 48, 410, and 75 m^2 g^{-1} respectively. The micro and total pore volumes were 0.19 and 0.56 cm^3 g^{-1}, respectively. The micro surface area and pore volume of conventional H-MCM-49 were similar to those of the zeolites reconstructed from NaY. Additionally, the number of acid sites in conventional H-MCM-49 zeolite was as follows: 402 μmol g^{-1} for Brønsted acid sites and 189 μmol g^{-1} for Lewis acid sites at 200 °C; 375 μmol g^{-1} for Brønsted acid sites and 168 μmol g^{-1} for Lewis acid sites at 350 °C. The texture and acidic properties of conventional H-MCM-49 were close to those of HYM500, and lower than those of HYM300. Table 4 gives the detailed alkylation performance of conventional H-MCM-49 from 200 to 260 °C. The HYM300 catalyst showed higher ethylene conversion and EB selectivity than the conventional H-MCM-49 catalyst at low reaction temperatures. The increase in ethylene conversion for HYM300 was different from that for the conventional H-MCM-49 catalyst, and unlike the conventional H-MCM-49 catalyst, HYM300 exhibited small changes in ethylene conversion as the temperature changed, which indicates that the active centers in HYM300 were very accessible.

Table 4 Ethylene conversion and EB selectivity over conventional H-MCM-49 catalyst[a]

Temperature (°C)	200	210	220	230	240	250	260
Ethylene conversion (%)	96.58	97.21	97.94	98.25	98.50	98.61	99.23
EB selectivity (%)	95.42	95.26	95.10	95.14	95.10	94.80	94.95

[a] Liquid-phase alkylation conditions: catalyst, 8 mL, $T = 200$ to 260 °C, $p = 3.5$ MPa, benzene $WHSV^{-1} = 3.0\ h^{-1}$, benzene/ethylene molar ratio = 12.0.

The results also confirm that an excellent catalyst that is smaller with high relative crystallinity, high BET surface area and a larger number of active centers, can produce a significant breakthrough in activity without loss of selectivity. Thus, the topology reconstruction of zeolites can achieve the size-controlled synthesis of target zeolites, and also prevent the trade-off between ethylene conversion and EB selectivity because of the better accessibility of active centers in the HYM300 catalyst.

According to our results, we can summarize the effects of the NaY zeolite size on the topology reconstruction, chemical and physical properties, size, and acidity of H-type zeolites. Smaller parent NaY zeolites improved the diffusion of the reactants on the NaY zeolites during the topology reconstruction, and also the relative crystallinity, the BET surface areas owing to the increase in external surface areas, and the number of acid sites. Most importantly, ethylene conversion and EB selectivity were improved by decreasing the size of parent NaY zeolites because of the better accessibility of the active centers on small H-type catalysts. In particular, HYM300 showed the highest value for both the ethylene conversion and EB selectivity. We successfully controlled the sizes of the target zeolites to improve the accessibility of active centers through topology reconstruction from smaller parent zeolites.

Thus, we show that size-controlled synthesis of MWW zeolites *via* topology reconstruction of parent NaY zeolites with different sizes is a potential method to improve both ethylene conversion and EB selectivity. In the topology reconstruction, we emphasize that size-controlled synthesis of MWW zeolites can be achieved for smaller zeolite catalysts, which possess a larger number of active centers and allow better access for benzene because diffusion is less limited. Furthermore, the higher relative crystallinity may lead to higher regularity for smaller-sized zeolites, and this may improve selectivity in alkylation. Our results may highlight a new strategy for enhancing both the catalytic activity and selectivity and this synthesis method should be applicable to many reactions that are diffusion limited and require reactions to occur on the external surface area.

4. Conclusion

MCM-49 zeolites with different sizes were synthesized *via* topology reconstruction from NaY zeolites with different sizes (1000, 500 and 300 nm). The size-controlled synthesis of target MCM-49 zeolites was achieved by selecting parent NaY zeolites with different sizes, regardless of volume increase. The effects of size on the topology reconstruction, texture properties and acidity of H-type zeolites were observed. Smaller parent NaY zeolites improved the diffusion of reactants on the parent zeolites during the topology reconstruction, and also the relative crystallinity, BET surface areas, external pore volumes and number of acid sites determined by Py-FTIR. This indicates that the smaller MCM-49 possessed a larger number of active centers (12 MR cups) on the outer surface and allowed better accessibility to active centers for benzene. The most promising result was the simultaneous improvement of both the ethylene conversion and EB selectivity as the size of the zeolites decreased, because the diffusion of the reactant over smaller H-type catalysts improved. In particular, HYM300 showed the highest ethylene conversion and EB selectivity. This demonstrates that smaller MWW zeolites and higher geometrical regularities can ensure excellent catalytic performance in the liquid-phase alkylation of benzene with ethylene. This alkylation performance may indicate a new strategy for enhancing both catalytic activity and selectivity, and our method should be applicable to many diffusion-limited or surface reactions.

Acknowledgements

This work was supported by the National Basic Research Program of China (973 Program, no. 2012CB224805). Special thanks to the Department of Analysis in Research Institute of Petroleum Processing Sinopec.

References

1 B. Yilmaz and U. Muller, *Top. Catal.*, 2009, **52**, 888–895.
2 B. Zhang, Y. J. Ji, Z. D. Wang, Y. M. Liu, H. M. Sun, W. M. Yang and P. Wu, *Appl. Catal., A*, 2012, **443–444**, 103–110.
3 J. Cejka, A. Vondrova, B. Wichterlova, G. Vorbeck and R. Fricke, *Zeolites*, 1994, **14**, 147–153.
4 C. Perego and P. Ingallina, *Catal. Today*, 2002, **73**, 3–22.
5 W. Vermeiren and J. P. Gilson, *Top. Catal.*, 2009, **52**, 1131–1161.
6 G. Bellussi, G. Pazzuconi, C. Perego, G. Girotti and G. Terzoni, *J. Catal.*, 1995, **157**, 227–234.
7 Y. C. Du, H. Wang and S. Chen, *J. Mol. Catal. A: Chem.*, 2002, **179**, 253–261.
8 J. C. Cheng, C. M. Smith and D. E. Walsh, *US Pat.*, 5,493,065, 1996.
9 J. C. Cheng, C. M. Smith, C. R. Venkat and D. E. Walsh, *US Pat.*, 5,600,048, 1997.

10 J. Cheng, T. Degnan, J. Beck, Y. Huang, M. Kalyanaraman, J. Kowalski, C. Loehr and D. Mazzone, *Stud. Surf. Sci. Catal.*, 1999, **121**, 53–60.
11 D. Y. Jan, J. A. Johnson, R. J. Schmidt and G. B. Woodle, *US Pat.*, 7,268,267 B2, 2007.
12 W. J. Roth and J. Cejka, *Catal. Sci. Technol.*, 2011, **1**, 43–53.
13 S. L. Lawton, A. S. Fung, G. J. Kennedy, L. B. Alemany, C. D. Chang, G. H. Hatzikos, D. N. Lissy, M. K. Rubin, H. K. C. Timken, S. Steuernagel and D. E. Woessner, *J. Phys. Chem.*, 1996, **100**, 3788–3798.
14 W. J. Roth and D. L. Dorset, *Microporous Mesoporous Mater.*, 2011, **142**, 32–36.
15 L. M. Rohde. G. J. Lewis, M. A. Miller, J. G. Moscoso, J. L. Gisselquist, R. L. Patton, S. T. Wilson and D. Y. Jan, *US Pat.*, 6,756,030 B1, 2004.
16 L. Puppe and J. Weiser, *US Pat.*, 4,439,409, 1984.
17 G. Perego, M. G. Clerici and A. Giusti, European Patent Application, 193032, 1988.
18 S. I. Zones, D. I. Holtermann, R. A. Innes, T. A. Pecoraro, D. S. Santilli and J. N. Ziemer, *US Pat.*, 4,826,667, 1989.
19 P. Ayrault, J. Datka, S. Laforge, D. Martin and M. Guisnet, *J. Phys. Chem. B*, 2004, **108**, 13755–13763.
20 H. W. Du and D. H. Olson, *J. Phys. Chem. B*, 2002, **106**, 395–400.
21 X. Y. Yin, N. B. Chu, J. H. Yang, J. Q. Wang and Z. F. Li, *Catal. Commun.*, 2014, **43**, 218–222.
22 C. T. W. Chu, C. T. Kresge, W. J. Roth, K. G. Simmons and J. C. Vartuli, *US Pat.*, 5,292,698, 1994.
23 M. Kaldstroma, N. Kumara, T. Heikkilab and D. Yu. Murzina, *Appl. Catal., A*, 2011, **397**, 13–21.
24 W. J. Roth, P. Chlubná, M. Kub and D. Vitvarová, *Catal. Today*, 2013, **204**, 8–14.
25 S. Inagaki, H. Imai, S. Tsujiuchi, H. Yakushiji, T. Yokoi and T. Tatsumi, *Microporous Mesoporous Mater.*, 2011, **142**, 354–362.
26 H. Xu, L. Y. Fu, J. G. Jiang, M. Y. He and P. Wu, *Microporous Mesoporous Mater.*, 2014, **189**, 41–48.
27 B. Onida, L. Borello, B. Bonelli, F. Geobaldo and E. Garrone, *J. Catal.*, 2003, **214**, 191–199.
28 J. Aguilar, S. B. C. Pergher, C. Detoni, A. Corma, F. V. Melo and E. Sastre, *Catal. Today*, 2008, **133–135**, 667–672.
29 V. Machadoa, J. Rochab, A. P. Carvalhoc and A. Martinsa, *Appl. Catal., A*, 2012, **445–446**, 329–338.
30 K. F. Liu, S. J. Xie, G. L. Xu, Y. N. Li, S. L. Liu and L. Y. Xu, *Appl. Catal., A*, 2010, **383**, 102–111.
31 K. F. Liu, S. J. Xie, H. J. Wei, X. J. Li, S. L. Liu and L. Y. Xu, *Appl. Catal., A*, 2013, **468**, 288–295.
32 I. Guray, J. Warzywoda, N. Bac and A. Sacco Jr, *Microporous Mesoporous Mater.*, 1999, **31**, 241–251.
33 S. L. Lawton, A. S. Fung, G. J. Kennedy, L. B. Alemany, C. D. Chang, G. H. Hatzikos, D. N. Lissy, M. K. Rubin, H. C. Timken, S. Steuernagel and D. E. Woessner, *J. Phys. Chem.*, 1996, **100**, 3788–3798.
34 Y. C. Shi, E. H. Xing, X. Z. Gao, D. Y. Liu, W. H. Xie, F. M. Zhang, X. H. Mu and X. T. Shu, *Microporous Mesoporous Mater.*, 2014, **200**, 269–278.
35 E. H. Xing, X. Z. Gao, W. H. Xie, F. M. Zhang, X. H. Mu and X. T. Shu, *RSC Adv.*, 2014, **4**, 24893–24899.
36 D. Vuono, L. Pasqua, F. Testa, R. Aiello, A. Fonseca, T. I. Koranyi and J. B. Nagy, *Microporous Mesoporous Mater.*, 2006, **97**, 78–87.